Journal of Molecular Catalysis A: Chemical 387 (2014) 147–155

Contents lists available at ScienceDirect

Journal of Molecular Catalysis A: Chemical

journal homepage: www.elsevier.com/locate/molcata

# Ethylbenzene dehydrogenation in the presence of carbon dioxide over magnesia-supported iron oxides

Maria do Carmo Rangel[a,*,1], Ana Paula de Melo Monteiro[a], Sergio Gustavo Marchetti[b], Sirlene Barbosa Lima[a], Márcia de Souza Ramos[a]

[a] GECCAT Grupo de Estudos em Cinética e Catálise, Instituto de Química, Universidade Federal da Bahia, Campus Universitário de Ondina, Federação, 40170-290 Salvador, BA, Brazil
[b] CINDECA, Facultad de Ciencias Exactas, Universidad Nacional de La Plata, La Plata, Argentina

ARTICLE INFO

*Article history:*
Received 14 November 2013
Received in revised form 6 February 2014
Accepted 1 March 2014
Available online 10 March 2014

*Keywords:*
Ethylbenzene
Styrene
Magnesium oxide
Iron oxide nanoparticles
Carbon dioxide

ABSTRACT

In recent years, several works have been addressed to decrease carbon dioxide emission or to capture, to storage and to use it. An attractive option is its use as feedstock of chemical industry, especially in dehydrogenation reactions (such as ethylbenzene dehydrogenation to produce styrene), providing an exothermic process which can be operated at lower temperatures, making negligible the cracking products. Aiming to find alternative catalysts for this reaction, magnesia-supported iron oxides were studied, being prepared by two different methods. The classical impregnation produced a spinel ($MgFe_2O_4$) co-existing with magnesia containing $Fe^{3+}$ species, this catalyst showing higher specific surface area and being more active and selective than magnesia. Moreover, the deposition of iron nanoparticles through a magnetic fluid on magnesia produced magnesia-supported hematite nanoparticles co-existing with magnesia containing $Fe^{3+}$ species. In this case, the specific surface area and the activity were even higher and the solid is much more reducible than the other sample. These findings were associated to hematite nanoparticles and to the lower tendency of iron species to diffuse into magnesia lattice. They show that the $Fe^{3+}$ species are more active and selective to styrene as hematite nanoparticles than when they are in the environment of magnesium ferrite.



## 1. Introduction

In recent times, the applications of new technologies to capture and to use carbon dioxide have been extensively studied and discussed, aiming to overcome the harmful effects caused by this gas in the environment [1,2]. In fact, the greenhouse gases have increased the average temperature of the earth and are expected to cause catastrophic events in the future.

Although carbon dioxide is already used as feedstock in several chemical processes, this consumption is not enough to significantly reduce its amount in the environment and thus new technologies or improvements are required. Carbon dioxide can be conveniently used as solvent and/or as reactants, providing carbon and/or oxygen for the synthesis of chemicals through various processes. Several works, for instance, have shown the use of carbon dioxide as oxidant in dehydrogenation of ethane [3], propane [4], isobutene [5] and ethylbenzene [6,7], as well as in methane dry reforming [8] and oxidative coupling of methane [9].

The use of carbon dioxide is especially advantageous in hydrocarbons dehydrogenation. These reactions are often reversible and thermodynamically equilibrium limited, being performed at high temperatures to increase the conversion. Under this condition, however, hydrocarbons cracking occur, decreasing the selectivity of the process. These difficulties can be overcome by carrying out an oxidation reaction using an oxidant and a catalyst, in which case the conversion is not strongly limited by thermodynamic factors. In addition, the reaction becomes exothermic and can be performed at low temperatures, making negligible the cracking products. Among the oxidizing agents most commonly used, carbon dioxide has been shown to be the most promising one to be used in dehydrogenation reactions [10,11].

The ethylbenzene dehydrogenation to produce styrene is one of the most representative examples of the improvement of the dehydrogenation process, by the use of carbon dioxide. In this case, the replacement of steam by carbon dioxide leads to a consumption of $1.5–1.9 \times 10^8$ instead of $1.5 \times 10^9$ cal per mol of styrene produced and the obtained hydrogen is removed as steam by the reverse

* Corresponding author. Tel.: +55 71 3283 6867; fax: +55 71 3237 4117.
*E-mail addresses:* mcarmov@ufba.br, mcarmov@gmail.com (M.d.C. Rangel).
[1] To whom the correspondence should be addressed.

http://dx.doi.org/10.1016/j.molcata.2014.03.002
1381-1169/

water gas shift reaction shifting the equilibrium to the dehydrogenation products. In addition, carbon dioxide removes the coke deposits produced during reaction [12,13]. These advantages contrast with the drawbacks of the classical process to produce styrene, by ethylbenzene dehydrogenation in the presence of steam, an endothermic and equilibrium limited reaction. As a result, the typical conversion is low, rarely exceeding 50%, even in processes performed at high temperatures. Side reactions also occur, leading to the production of toluene, benzene and coke which affect the yield of the process and may lead to catalyst deactivation [14,15]. In spite of these problems, this process is responsible for the supply of 90% of the global production of styrene (around $13 \times 10^6$ t/year) [14], which is one of the most used chemical for the manufacture of synthetic rubbers, plastics and resins copolymers, among other products of high commercial value.

Because of the advantages of the use of carbon dioxide in ethylbenzene dehydrogenation, a lot of work has been addressed to find efficient catalysts for this process. Since the first works [14,16–18], it was noted that the commercial catalysts based on iron oxide are not suitable for ethylbenzene dehydrogenation in the presence of carbon dioxide. Since that time, extensive studies have been carried out in order to find new or modified catalysts that can be effective in the presence of carbon dioxide. Iron oxide promoted with alkali metals supported on alumina or activated carbon [17–21], zeolites or zirconia-supported iron oxide [22,23], vanadium oxide and vanadium–antimony supported on alumina [24,25], among other catalysts, have been evaluated and proven to be effective to produce styrene. These studies have shown that the effect of carbon dioxide on the activity, selectivity and stability of the catalyst for ethylbenzene dehydrogenation depends on the chemical nature of these solids. Activated carbons-based catalysts have also proved to be active in ethylbenzene dehydrogenation in the presence of carbon dioxide [6,26,27].

In a previous work [7], we have found that metal oxides such as lanthana ($La_2O_3$), magnesia (MgO), niobia ($Nb_2O_5$), titania ($TiO_2$) and zirconia ($ZrO_2$) are active and selective catalysts for ethylbenzene dehydrogenation in the presence of carbon dioxide to produce styrene. In the present work, we have combined the activity of iron oxides with the basicity of magnesia in order to find efficient catalysts for this reaction. For this purpose, magnesia-supported iron oxides were prepared by different methods and evaluated in ethylbenzene dehydrogenation in the presence of carbon dioxide.

## 2. Experimental

### 2.1. Catalysts preparation

The support was prepared by adding 250 mL of a magnesium nitrate solution (1 mol $L^{-1}$) simultaneously with an ammonium hydroxide solution (8.5%) to a beaker containing water, under stirring at room temperature. After complete addition of the reactants, the pH was adjusted to 10 by the addition of a concentrated ammonium hydroxide solution (30%). After aging the sol for 24 h under stirring, the system was centrifuged and the obtained gel was washed with water, this procedure was repeated six times until no chloride ion was detected in the supernatant. The gel was dried at 120 °C for 12 h, ground and sieved in 100 mesh. The material obtained was heated (10 °C $min^{-1}$) under air flow (50 mL $min^{-1}$) up to 750 °C and kept at this temperature for 5 h to get the M sample.

For the preparation of magnesia-supported iron oxides (10% w/w), two preparation methods were used: the conventional impregnation and the deposition of iron oxide nanoparticles through a magnetic fluid. In the conventional impregnation, the support was dispersed in an iron nitrate solution (5 mL per gram of support) and kept under stirring, for 4 h. The excess water was evaporated at 70 °C and the solid was dried at 120 °C, for 12 h. Then, the sample was calcined in the same conditions used for the support to obtain the IM sample.

In the second method, a suspension of iron oxide nanoparticles (magnetic fluid) was previously prepared. In this case, an aqueous solution with a molar ratio of Fe(II) to Fe(III) of 0.5 was obtained using ferric and ferrous chloride and hydrochloric acid, under stirring and nitrogen bubbling. Then a sodium hydroxide solution (1.5 mol $L^{-1}$) was dropped into the system. The supernatant was separated from the precipitate by centrifugation. After this, 500 mL of a hydrochloric acid solution (0.01 mol $L^{-1}$) was added under stirring to neutralize the anionic charge of the nanoparticles. The cationic colloidal nanoparticles were separated by centrifugation (4000 rpm) and peptized by the addition of water.

In order to deposit the nanoparticles on magnesia, the support was pretreated with water, the pH value was adjusted to approximately 3 and then concentrated nitric acid was dropped into the system. The support was then immersed into the magnetic fluid (5 mL per gram of support) and kept for 2 h, under stirring. After this time, the system was centrifuged and the solid was dried for 30 min. Again, the support was kept in contact with the fluid and then centrifuged. These steps were repeated five times and finally the material was dried in an oven at 120 °C, for 12 h. The solid was calcined in the same conditions used for the supports to get the INM sample.

### 2.2. Samples characterization

The samples were characterized by thermogravimetry (TG), differential thermal analysis (DTA), X-ray diffraction (XRD), chemical analysis, specific surface area (Sg) and porosity measurements, Mössbauer spectroscopy and temperature programmed reduction (TPR).

The experiments of thermogravimetry and differential thermal analysis were performed in a Mettler Toledo model TGA/SDTA851 equipment. During the analysis, 0.006 g of sample was heated from 25 to 1000 °C, at a heating rate of 10 °C $min^{-1}$, under air flow (50 mL $min^{-1}$). The X-ray diffraction analyses were carried out in XD3A Shimadzu equipment, using Cu $K\alpha$ radiation generated at 40 kV and 30 mA with a nickel filter. The data were collected over a $2\theta$ range of 5–80°, with a step size of 0.02°, at a scanning rate of 2° $min^{-1}$.

The iron concentration in the catalysts was determined by atomic absorption spectrophotometry in a Varian model SpectrAA 220 equipment using a hollow cathode lamp iron. The samples were previously digested in an open vessel, using a hydrochloric acid solution (75% v/v) and heated up to boiling, being kept at this temperature for 10 min.

The specific surface area (Sg) and porosity of the calcined solids were measured by nitrogen adsorption/desorption at −196 °C by BET and BJH methods, respectively, using a Micromeritics model ASAP 2010 instrument. Before the analysis, the sample (0.2 g) was heated up to 200 °C under vacuum (2 μmHg) to remove water from the solid.

The Mössbauer spectra were obtained in a spectrometer equipped with twelve channels with constant acceleration and geometry of transmission. A source of $^{57}Co$ was used in a matrix of Rh of 50 me normal. All isomeric shifts were related for a standard at 25 °C. For each component of the spectra, Lorentzians lines of the same width were used. All the spectra were fitted and were obtained the distributions of the hyperfine parameter for quantify the different phase of the iron oxides. The spectra were obtained at room temperature and folded to minimize geometric effects, being evaluated using a commercial computer fitting program named Recoil.

The curves of temperature programmed reduction profiles of the samples were obtained on calcined samples (0.0350 g) in a Micromeritics model TPD/TPO 2900 equipment, using a 5% $H_2/N_2$ mixture. Before the analysis, the sample was heated under nitrogen flow (60 mL $min^{-1}$) at 10 °C $min^{-1}$ until 160 °C, for 30 min to remove water and other impurities. The analysis was performed by heating the sample from room temperature up to 1000 °C under a heating rate of 10 °C $min^{-1}$ and a flow (60 mL $min^{-1}$) of the gas mixture.

### 2.3. Catalysts evaluation

The catalyst and the support were evaluated in ethylbenzene dehydrogenation in the presence of carbon dioxide, using an ethylbenzene to carbon dioxide molar ratio of 10. The reaction was performed at atmospheric pressure and 600 °C over a catalyst bed (0.3 g), for 6 h. During the experiments, a nitrogen flow (20 mL $min^{-1}$) was bubbled into a saturator containing ethylbenzene at 77 °C, so that $3.33 \times 10^{-5}$ mol of ethybenzene (0.80 mL $min^{-1}$) was vaporized and then a carbon dioxide to etylbenzene molar ratio of 10 was obtained. Carbon dioxide (8 mL $min^{-1}$) was then mixed with nitrogen containing ethylbenzene and the resulting stream was fed to the reactor. The reactor effluent was analyzed by on line gas chromatograph. At the end of each run, the reactor was cooled to room temperature under nitrogen flow. The reaction conditions were adjusted to eliminate the diffusion limitations. The spent catalysts were characterized by X-ray diffraction, specific surface area measurements and Mössbauer spectroscopy.

## 3. Results and discussion

### 3.1. Thermogravimetry and differential thermal analysis

Fig. 1(a) shows the thermogravimetry curves for the samples before calcination. The curve for the magnesia precursor (M sample) (Fig. 1a) showed a weight loss below 130 °C, related to the loss of physically adsorbed compounds. It can also be noted a strong weight loss in the range of 310 to 400 °C, assigned to the decomposition of magnesium hydroxide to form magnesium oxide, which occurs in one step [28]. A small weight loss between 400 and 550 °C is related to the decomposition of the largest particles of magnesium hydroxide [29]. The IM sample shows a weight loss in a single step in the range of 280 and 580 °C, which can be associated to the production of iron and/or magnesium compounds. The precursor of magnesia-supported nanoparticles (INM sample) also presents a weight loss in a single step, but in a narrower range of temperature, between 400 and 625 °C, which is also related to the production of iron and/or magnesium compounds. All these events are endothermic as shown in Fig. 1b.

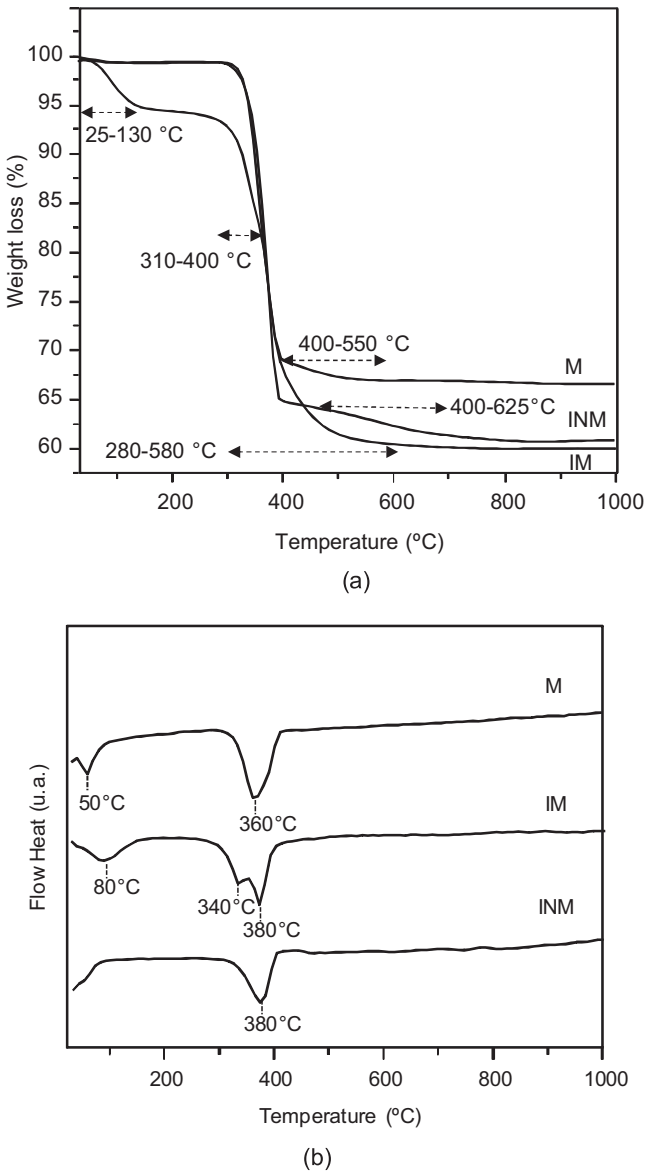


**Fig. 1.** Curves of (a) thermogravimetry and of (b) differential thermal analysis for the precursors of the support and of the catalysts. I—iron; M—magnesia; N—nanoparticle.

### 3.2. X-ray diffraction

The XRD patterns of the samples are shown in Fig. 2. As we can see, the support (M sample) shows the diffration profile of the periclase phase of magnesia (JCPDS 87-0652). After ethylbenzene dehydrogenation, the same phase was noted and no significant widening or narrowing of the peaks was observed. It means that there was no change in the crystallinity and/or in the particle size, indicating that this catalyst was stable during reaction.

The profiles of the X-ray diffractograms for the iron oxide-containing samples, displayed in Fig. 2, also show the presence of the periclase phase of magnesia (JCPDS 87-0652) for all catalysts. In addition, it can be noted the presence of hematite (JCPDS 87-1166) and magnesium ferrite, $MgFe_2O_4$ (JCPDS 73-1960) for fresh catalysts, regardless the method of iron incorporation. During ethylbenzene dehydrogenation, hematite went on phase change to produce magnetite (JCPDS 87-2334) as shown by the spent catalysts (Fig. 2b). These findings are in accordance with previous studies [30–32] for hematite-based catalysts containing different dopants. Furthermore, magnesia and some magnesium ferrite were detected for the spent catalysts. All samples showed the same behavior independently of the preparation method of the catalysts, meaning that magnesia did not affect the change phase from hematite to magnetite.

### 3.3. Chemical analysis

The chemical analysis results for the samples are shown in Table 1. It can be noted that the iron concentrations were higher than the nominal one (10% w/w), suggesting that some support was lost during the impregnation step.

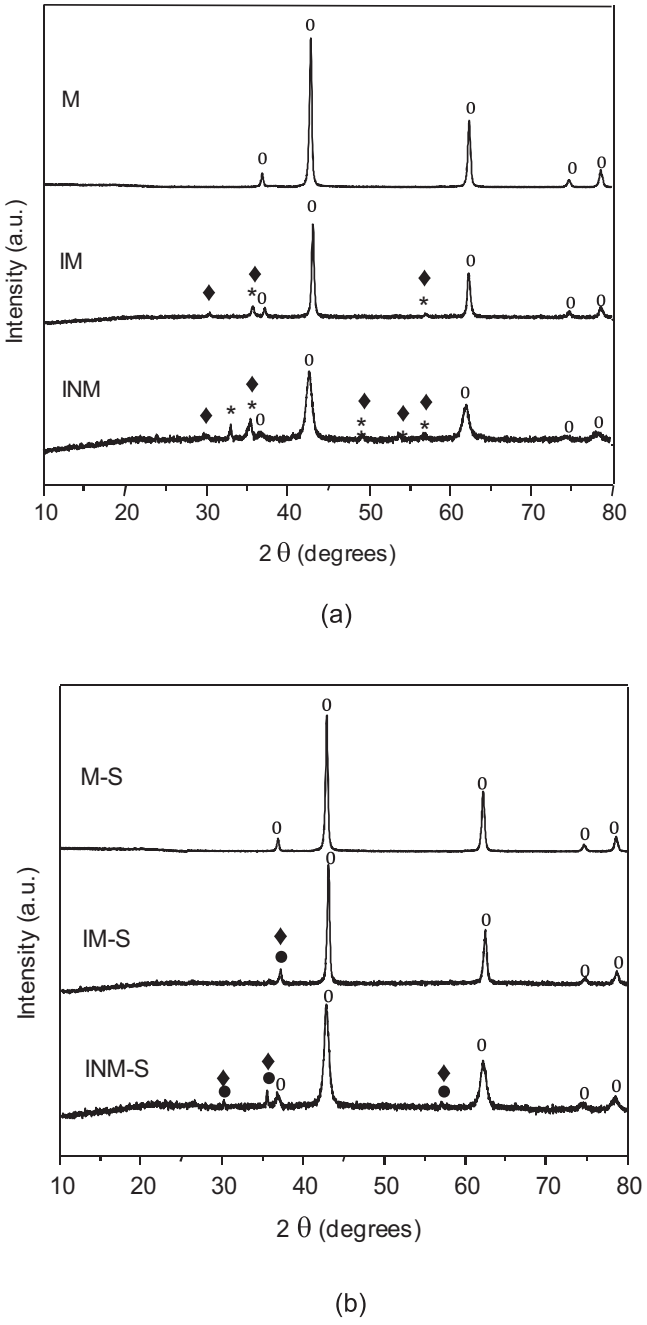


**Fig. 2.** X-ray diffraction for the (a) fresh and (b) spent catalysts. I—iron; M—magnesia; N—nanoparticle. (*) hematite; ($_o$) periclase; (●) magnetite; (♦) magnesium ferrite.

### 3.4. Specific surface area and porosity measurements

The adsorption/desorption isotherms for the support and for the catalysts are shown in Fig. 3. All solids show a Type 3 isotherm, typical of macroporous solids with a small type H3 hysteresis loop, indicating the presence of mesopores in the samples.

Table 1 displays the specific surface areas of the catalysts before and after ethylbenzene dehydrogenation. It can be noted that the addition of iron to magnesia led to an increase of the specific surface area, this effect is much more important for the sample prepared by the deposition of iron oxide nanoparticles. After ethylbenzene dehydrogenation, all specific surface areas were lower than those of the fresh catalysts, indicating the coalescence of particle and pores. This effect was more important for the iron-containing samples, probably due to the change phase of hematite to magnetite, which was found to be followed by coalescence of particles and pores [32–34].

The curves of pores distribution (Fig. 4) show that magnesia displays an unimodal distribution with meso and macropores between 20 and 224 nm with a maximum at around 77 nm. The incorporation of iron oxide by the classical method (IM sample) shifted the curve and made the distribution wider, between 4 and 300 nm, with a maximum at about 52 nm. On the other hand, the incorporation of iron oxide to magnesia through a magnetic fluid (INM sample) produced a solid with a bimodal distribution with mesopores between 2.2 and 50 nm with a maximum at around 3.8 and macropores between 50 and 280 nm with a maximum at about 82 nm. These findings are closely related to the specific surface areas of the solids. The slight increase found for IM sample, as compared to pure magnesia, is mainly related to the shift of the modal pore distribution to small values of pore diameters. On the other hand, the large increase noted for the INM sample is probably due to the bimodal distribution related to a larger contribution of mesopores.

**Table 1**
Elemental chemical composition and specific surface areas for the support and for the catalysts before (Sg) and after (Sg*) ethylbenzene dehydrogenation.

| Samples | $Fe_2O_3$ (% w/w) | Sg ($m^2\ g^{-1}$) | Sg* ($m^2\ g^{-1}$) |
|---|---|---|---|
| M | – | 21 | 18 |
| IM | 12.66 | 28 | 22 |
| INM | 11.98 | 126 | 84 |

I—iron; M—magnesia; N—nanoparticle.

### 3.5. Mössbauer spectroscopy

The Mössbauer spectra for the fresh and spent catalysts are shown in Fig. 5 while Tables 2 and 3 display the hyperfine parameters for the fresh and spent catalysts, respectively. For the IM sample, the spectrum obtained at 298 K was fitted with two sextuplets and one doublet. The two sextuplets have hyperfine parameters assignable to $Fe^{3+}$ ions located in the octahedral (B site) and tetrahedral (A site) sites of magnesium ferrite ($MgFe_2O_4$) spinel [35]. The doublet can be assigned to paramagnetic $Fe^{3+}$ ions (e.g. isolated ions diffused in magnesia lattice) or superparamagnetic species (sp) of $Fe^{3+}$ (e.g. $MgFe_2O_4$ (sp) and/or α-$Fe_2O_3$ (sp)). In order to distinguish between these possibilities, the spectrum at 30 K was also obtained (Fig. 5). This spectrum was fitted with two sextuplets and one doublet. It can be noted that the hyperfine parameters of these sextuplets are assignable to $Fe^{3+}$ ions located in the octahedral (B site) and tetrahedral (site A) sites of $MgFe_2O_4$ spinel [35]. By considering that the doublet area decreased by approximately 11% (46 ± 1% at 298 K vs. 35 ± 4% at 30 K) and that there was no new magnetic signal assignable to other species besides $MgFe_2O_4$ spinel, it can be concluded that this 11% correspond to a fraction of very small particles of this compound which are in regimen of superparamagnetic relaxation at 298 K. The remaining 35% were kept as a doublet even at a temperature as low as 30 K and did not show any sign of the beginning of magnetic blocking as would be, for instance, if there is a curved background. For this reason, one can conclude that for the IM sample 35 ± 4% of paramagnetic $Fe^{3+}$ ions have diffused into magnesia lattice.

For the INM sample, the Mössbauer spectrum measured at 298 K was fitted with two sextuplets: one of them magnetically blocked and the another relaxing one. The magnetically blocked sextet has hyperfine parameters of hematite, α-$Fe_2O_3$ [36]. The second sextet is difficult to assign because of its relaxing behavior and thus it was necessary to obtain the spectrum at low temperature to complete the assignment. The spectrum measured at 30 K was fitted with two sextuplets and a doublet. The spectrum with the

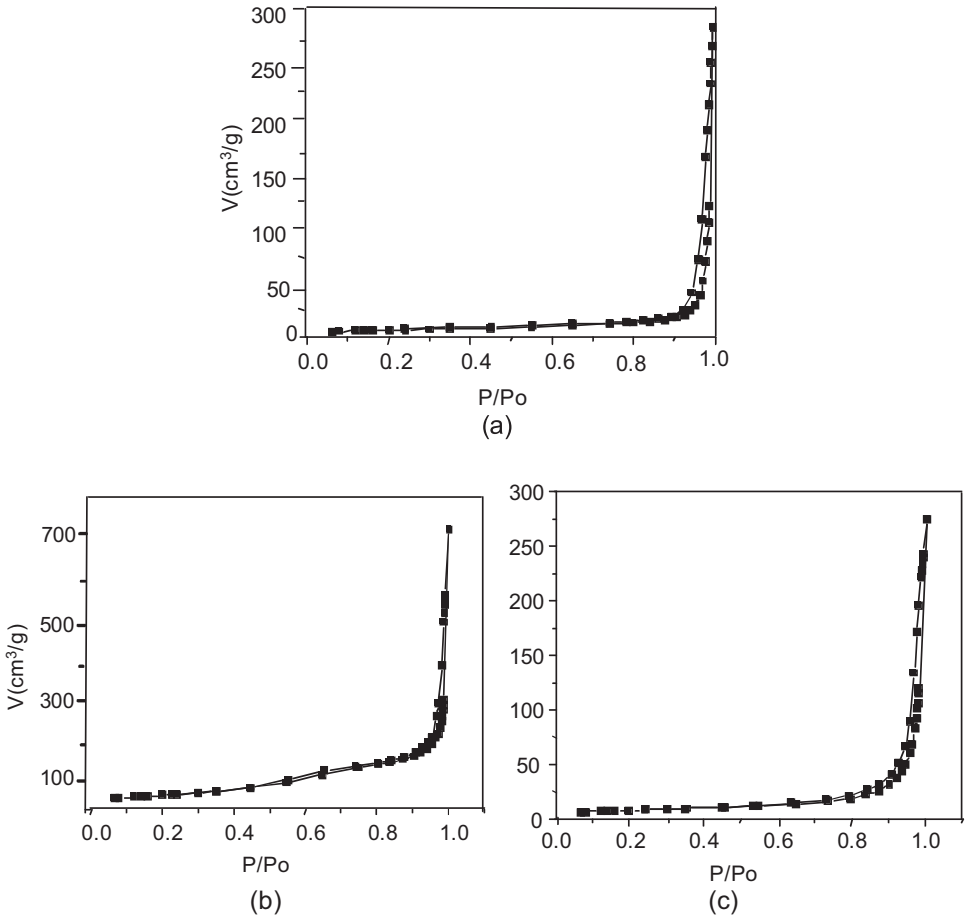


**Fig. 3.** Adsorption and desorption isotherms for the (a) M; (b) IM and (c) INM samples. I—iron; M—magnesia; N—nanoparticle.

largest hyperfine field corresponds to hematite that underwent the Morin transition and thus has a crystallite size greater than 20 nm [36]. The second sextet can also be assigned to hematite but that did not undergo the Morin transition, since the value of $2\varepsilon$ was almost null and then the particles are smaller than 20 nm. This fraction of hematite corresponds to the relaxing signal at room temperature. The possibility of the second sextet can be assigned to $Fe^{3+}$ ions in B sites of $MgFe_2O_4$ spinel can be discarded, since the corresponding signal related to $Fe^{3+}$ ions in A sites was not detected. The small doublet which was not magnetically blocked at 30 K can be assigned to a small fraction of paramagnetic $Fe^{3+}$ ions diffused in magnesia lattice.

**Table 2**
Hyperfine parameters for the fresh catalysts.

| Species | Parameters | $T$ = 298 K | | $T$ = 30 K | |
|---|---|---|---|---|---|
| | | IM | INM | IM | INM |
| $\alpha$-$Fe_2O_3$ | $H$ (T) | – | 51.26 ± 0.04 | – | 54.24 ± 0.03 |
| | $\delta$ (mm/s) | – | 0.36 ± 0.01 | – | 0.49 ± 0.01 |
| | $2\varepsilon$ (mm/s) | – | −0.21 ± 0.01 | – | 0.40 ± 0.01 |
| | % | – | 36 ± 1 | – | 45 ± 1 |
| Relaxing ($\alpha$-$Fe_2O_3$) | $H$ (T) | – | 44 ± 2 | – | 51.35 ± 0.09 |
| | $\delta$ (mm/s) | – | 0.29 ± 0.03 | – | 0.40 ± 0.01 |
| | $2\varepsilon$ (mm/s) | – | 0 (*) | – | −0.02 ± 0.02 |
| | % | – | 64 ± 2 | – | 49 ± 1 |
| $Fe^{3+}$ in B sites of $MgFe_2O_4$ | $H$ (T) | 44.7 ± 0.2 | – | 52.5 ± 0.2 | – |
| | $\delta$ (mm/s) | 0.31 (*) | – | 0.49 ± 0.03 | – |
| | $2\varepsilon$ (mm/s) | 0.01 ± 0.04 | – | 0.08 ± 0.04 | – |
| | % | 29 ± 1 | – | 27 ± 6 | – |
| $Fe^{3+}$ in A sites of $MgFe_2O_4$ | $H$ (T) | 40.3 ± 0.6 | – | 50.9 ± 0.3 | – |
| | $\delta$ (mm/s) | 0.27 (*) | – | 0.36 ± 0.02 | – |
| | $2\varepsilon$ (mm/s) | −0.06 ± 0.09 | – | −0.06 ± 0.03 | – |
| | % | 25 ± 1 | – | 38 ± 6 | – |
| Paramagnetic $Fe^{3+}$ and/or superparamagnetic $Fe^{3+}$ species | $\Delta$ (mm/s) | 0.72 ± 0.01 | – | 0.74 ± 0.01 | 0.63 ± 0.05 |
| | $\delta$ (mm/s) | 0.31 ± 0.01 | – | 0.43 ± 0.01 | 0.35 (*) |
| | % | 46 ± 1 | – | 35 ± 4 | 6 ± 1 |

I—iron; M—magnesia; N—nanoparticle. H: hyperfine magnetic field in Tesla; $\delta$: isomer shift referred to $\alpha$-Fe at 298 K, $2\varepsilon$: quadrupole shift; $\Delta$: quadrupole splitting, (*): parameter held fixed in fitting.

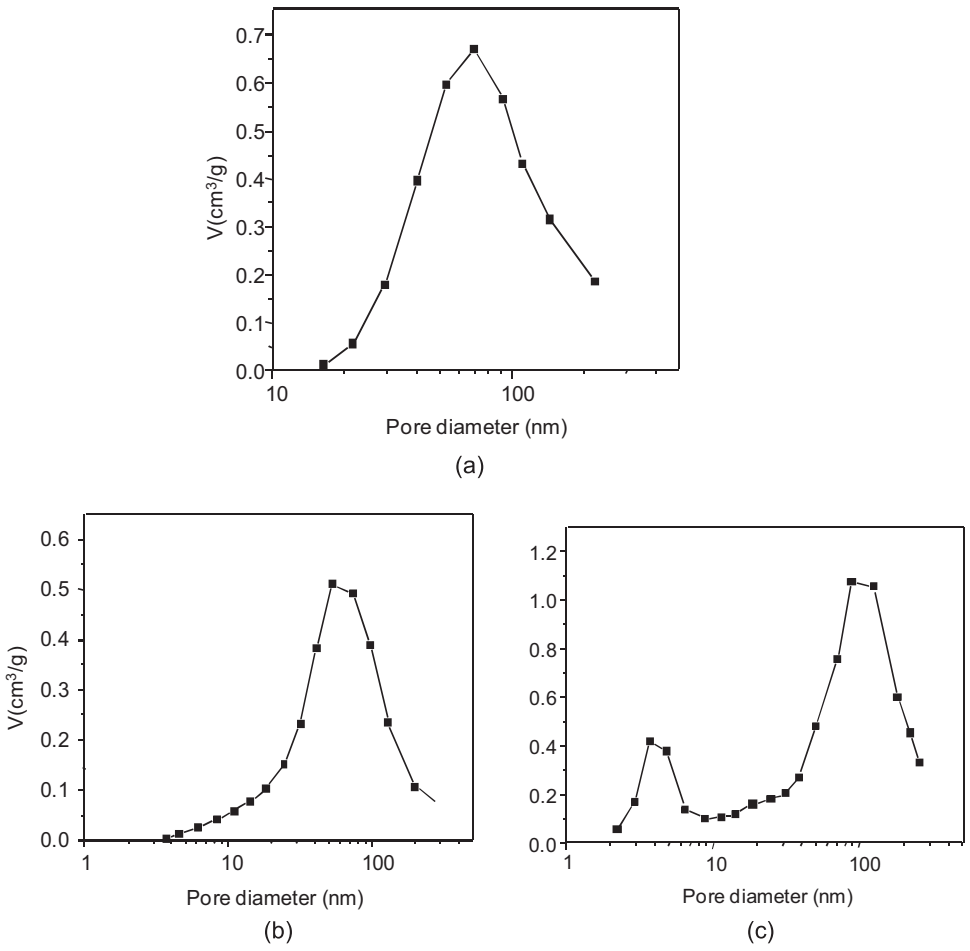


**Fig. 4.** Pore size distribution curves for the (a) M; (b) IM and (c) INM samples. I—iron; M—magnesia; N—nanoparticle.

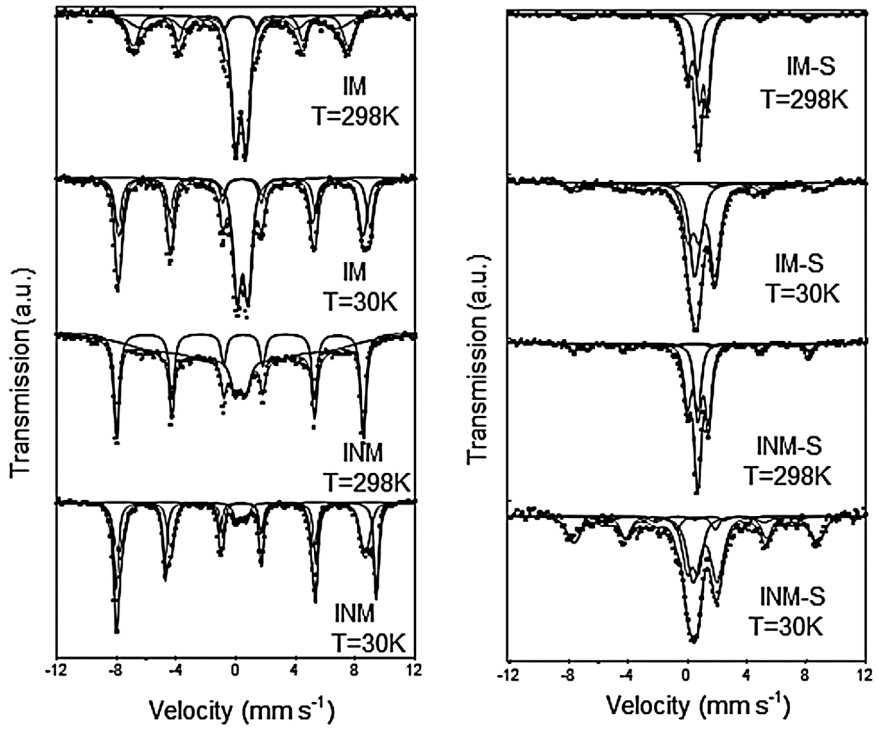


**Fig. 5.** Mössbauer spectra for the (a) fresh and (b) spent catalysts. I—iron; M—magnesia; N—nanoparticle.

**Table 3**
Hyperfine parameters for the spent catalysts.

| Species | | Parameters | | $T$ = 298 K | $T$ = 30 K |
|---|---|---|---|---|---|
| | | FMgU | NFMgU | FMgU | NFMgU |
| $Fe^{3+}$ in A sites of $Fe_3O_4$ | $H$ (T) | 49.3 ± 0.5 | 49.1 ± 0.3 | 50.4 ± 0.6 | 51.0 ± 0.4 |
| | $\delta$ (mm/s) | 0.32 ± 0.06 | 0.24 ± 0.04 | 0.55 (*) | 0.55 (*) |
| | $2\varepsilon$ (mm/s) | 0 (*) | 0 (*) | 0.2 ± 0.2 | 0.05 ± 0.09 |
| | % | 5 ± 1 | 12 ± 1 | 12 ± 2 | 32 ± 3 |
| $Fe^{"2.5+"}$ in B sites of $Fe_3O_4$ | $H$ (T) | 46.1 ± 0.6 | 46.5 ± 0.4 | 39.0 (*) | 39.0 (*) |
| | $\delta$ (mm/s) | 0.67 ± 0.07 | 0.72 ± 0.05 | 1.1 (*) | 1.1 (*) |
| | $2\varepsilon$ (mm/s) | 0 (*) | 0 (*) | −0.79 (*) | −0.79 (*) |
| | % | 5 ± 1 | 8 ± 1 | 5 ± 1 | 10 ± 3 |
| Paramagnetic $Fe^{3+}$ and/or superparamagnetic $Fe^{3+}$ species | $\Delta$ (mm/s) | 0.67 ± 0.02 | 0.70 (*) | 0.80 ± 0.03 | 0.76 ± 0.09 |
| | $\delta$ (mm/s) | 0.32 ± 0.01 | 0.33 (*) | 0.41 ± 0.02 | 0.34 ± 0.05 |
| | % | 39 ± 1 | 37 ± 1 | 30 ± 1 | 23 ± 2 |
| Paramagnetic $Fe^{2+}$ and/or superparamagnetic $Fe^{2+}$ species | $\Delta$ (mm/s) | 0.57 ± 0.01 | 0.72 (*) | 1.38 ± 0.02 | 1.62 ± 0.06 |
| | $\delta$ (mm/s) | 1.06 ± 0.01 | 1.04 (*) | 1.18 ± 0.01 | 1.20 ± 0.03 |
| | % | 51 ± 1 | 43 ± 1 | 53 ± 1 | 35 ± 2 |

I—iron; M—magnesia; N—nanoparticle. H: hyperfine magnetic field in Tesla; $\delta$: isomer shift referred to α-Fe at 298 K, $2\varepsilon$: quadrupole shift; $\Delta$: quadrupole splitting, (*): parameter held fixed in fitting.

The two fractions of hematite for the INM sample showed decreased hyperfine magnetic fields as compared to bulk hematite. This decrease can be attributed to crystal size effects and thus the model of collective magnetic excitations can be used to estimate the crystallite size [37]. By using a basal magnetic anisotropy constant ($K_{BU}$) of $1.3 \times 10^{-3}$ J m$^3$, suitable for hematite particles larger than 20 nm [38], it is possible to estimate the size of hematite particles, which are magnetically blocked to 298 K and undergo the Morin transition, using Eq. (1), where $H_{obs}$ is the magnetic hyperfine field of hematite species of the catalyst; $H_{bulk}$ is the magnetic hyperfine field of bulk hematite; $k_B$ is the Boltzmann constant; $T$ is the absolute temperature at which the spectrum was measured; $K$ is the constant of magnetic anisotropy and $V$ is the crystallite volume.

$$H_{obs} = H_{bulk}\left(1 - \frac{k_B T}{2KV}\right) \quad (1)$$

The value obtained for the particles size of INM sample was 71 nm. As predicted on basis of the Morin transition, the nanoparticles size was larger than 20 nm. When the model is applied to the other fraction of hematite species (which were magnetically blocked at 30 K and which did not undergo the Morin transition) the value obtained is 18 nm. This means that this fraction of nanoparticles is almost four times smaller than the other ones.

The Mössbauer spectra for the spent catalysts measured at 298 K (Fig. 5) were fitted with two doublets and two sextuplets. The two partially resolved sextuplets can be assigned to $Fe^{3+}$ ions located in tetrahedral sites (A sites) and to $Fe^{"2.5+"}$ in octahedral sites (site B) of magnetite ($Fe_3O_4$) [36]. The doublets can be assigned to paramagnetic $Fe^{3+}$ and $Fe^{2+}$ ions (e.g. isolated ions diffused in magnesia lattice) or to superparamagnetic (sp) $Fe^{3+}$ and $Fe^{2+}$ species (e.g. $MgFe_2O_4$ (sp) and/or $Fe_3O_4$ (sp)).

In order to distinguish between these possibilities, the spectra at 30 K were also obtained. They were fitted with two sextuplets and two doublets, the two sextuplets were assigned to magnetite. For this oxide, below the Verwey temperature (around 120 K), there are five sites for iron ions: tetrahedral sites, I-octahedral sites and II-octahedral for $Fe^{3+}$ ions and I-octahedral sites and II-octahedral sites for $Fe^{2+}$ ions. However, as this species is found in low percentage in this catalyst it is not reasonable to include so many interactions in the fitting. Because of this, two sites were used instead of five ones: each of them is a weighted average, according to the populations of each kind of ions: 28% of $Fe^{3+}$ ions in tetrahedral sites; 24% of $Fe^{3+}$ ions in I-octahedral sites; 23% of $Fe^{3+}$ ions in II-octahedral sites; 15% of $Fe^{2+}$ ions in I-octahedral sites and 10% of $Fe^{2+}$ ions in II-octahedral sites normalized to 100%. All values used were taken from the work of Berry et al. [39].

Regarding the doublets, they still represent a significant fraction at 30 K and thus the percentage of these signals detected at 30 K can be assigned to paramagnetic isolated $Fe^{3+}$ and $Fe^{2+}$ ions diffused into magnesia lattice. By comparing these values with those obtained at 298 K, it can be seen that there was a small decrease for the IM sample: 90 ± 2% at 298 K vs. 83 ± 2% at 30 K. Therefore, one can consider that these doublets at 298 K represent almost completely the paramagnetic ions. In contrast, the INM sample showed a more important decrease: 80 ± 2% at 298 K vs. 58 ± 4% at 30 K. Therefore, for the spent catalyst at room temperature the doublets have contributions of paramagnetic species and of superparamagnetic magnetite (the presence of other species can be discarded since only magnetically blocked magnetite was detected at 30 K).

In conclusion, the two methods of preparation generated different solids: the impregnation method followed by calcination led a reaction between iron nitrate and magnesia, producing magnesium ferrite as well as an important diffusion of paramagnetic $Fe^{3+}$ ions into magnesia lattice (35 ± 4%). On the other hand, the deposition of nanoparticles through a magnetic fluid and subsequent calcination resulted in the formation of two fractions of different sizes: hematite particles of around 71 and 18 nm and a very small percentage (6 ± 1%) of $Fe^{3+}$ ions diffused into magnesia lattice. During ethylbenzene dehydrogenation, the reducing atmosphere produces significant changes for both solids, which tend to contain the same species: magnetite and paramagnetic $Fe^{2+}$ and $Fe^{3+}$ ions diffused into magnesia lattice. However, there are still some differences: the amount of diffused ions is much larger for the spent IM sample: 83 ± 2% vs. 58 ± 4% for INM sample. Furthermore, there is a fraction of smaller magnetite nanoparticles in the INM sample, which shows superparamagnetic behavior at 298 K that was not present in the IM sample.

### 3.6. Temperature programmed reduction

The curves of temperature programmed reduction for magnesia-supported iron oxides are shown in Fig. 6. It can be noted that magnesia (M sample) showed a small peak centered at around 330 °C, which can be assigned to the reduction of nitrate ions, in agreement with previous works [29,40]. The IM sample shows a peak centered at 390 °C, which can be attributed to the reduction of $Fe^{3+}$ to $Fe^{2+}$ species [41,42] in magnesium ferrite. The peak at 470 °C can be related to the reduction of $Fe^{3+}$ to $Fe^{2+}$ species diffused in magnesia lattice and then in strong interaction with the support. On the other hand, the INM sample shows two peaks at 300 and 378 °C related to the reduction of $Fe^{3+}$ in hematite to $Fe^{2+}$ species in magnetite [8,32,34,42] on the surface and in the

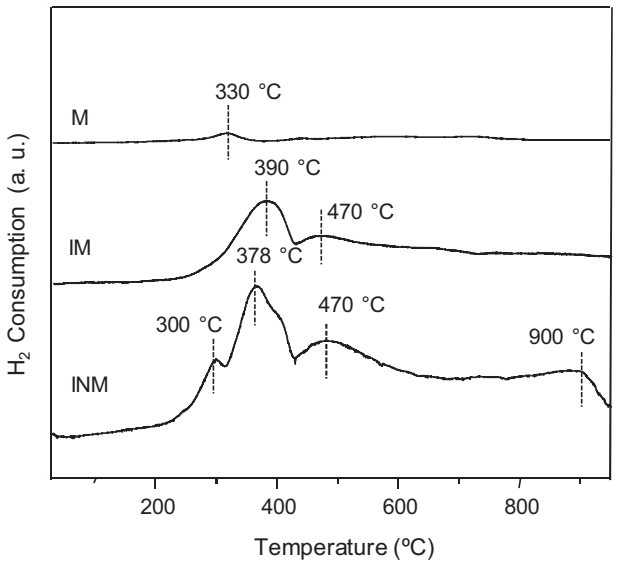


**Fig. 6.** Temperature programmed reduction curves for the catalysts. I—iron; M—magnesia; N—nanoparticle.

bulk, respectively as well as to the reduction of iron species in magnesium ferrite [41,42]. The peak at 900 °C can be assigned to the reduction of magnetite to metallic iron as found previously [8,32,34,42]. By comparing the iron-containing samples, one can see that the INM sample is more reducible than the IM sample. This finding can be explained by the results of Mössbauer spectroscopy, according to which most of $Fe^{3+}$ species are in magnesia ferrite or in diffused into magnesia lattice where they are expected to be difficult to be reduced. On the other hand, only a small fraction of $Fe^{3+}$ species is diffused into magnesia lattice and then the majority of iron is present and hematite nanoparticles, which are on the surface and easier to be reduced.

### 3.7. Activity and selectivity of the catalysts

Fig. 7 shows the ethylbenzene conversion as a function of reaction time. As we can see, magnesia itself is active in the reaction showing values close to that of the commercial catalyst (10%), evaluated in the presence of steam [43]. The addition of iron to

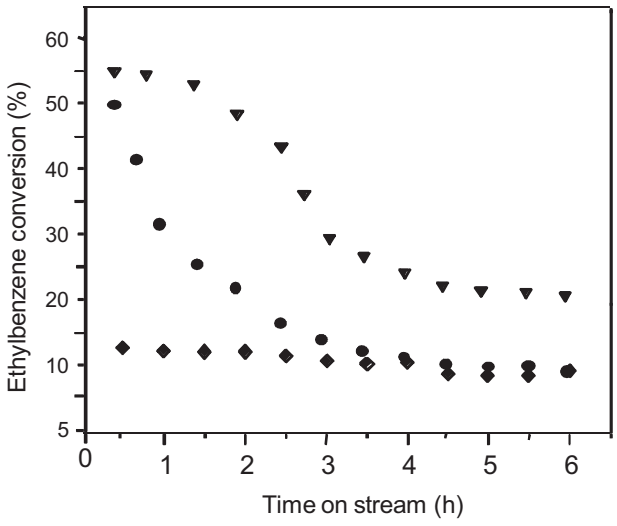


**Fig. 7.** Ethylbenzene conversion as a function of time obtained over the catalysts. (♦) M sample; (●) IM sample (▼) INM sample. I—iron; M—magnesia; N—nanoparticle.

**Table 4**
Ethylbenzene conversion ($X$), styrene selectivity ($S_{ST}$), styrene yield ($Y_{ST}$), benzene selectivity ($S_{BZ}$) and toluene selectivity ($S_{TOL}$) for the catalysts after 4 h on stream during ethylbenzene dehydrogenation in the presence of carbon dioxide.

| Samples | $X$ (%) | $S_{ST}$ (%) | $Y_{ST}$ (%) | $S_{BZ}$(%) | $S_{TOL}$(%) |
|---|---|---|---|---|---|
| M | 12 | 86 | 10 | 6.0 | 8.0 |
| IM | 12 | 93 | 11 | 2.0 | 5.0 |
| INM | 25 | 97 | 24 | 1.0 | 2.0 |

I—iron; M—magnesia; N—nanoparticle.

magnesia increased the activity even more, as we can see in the first hours of reaction, being the magnesia-supported iron nanoparticles the most active one. As found by Mössbauer spectroscopy, the IM sample is mostly made of magnesium ferrite and then it can be concluded that this compound is also active in the ethylbenzene dehydrogenation. However, it is less active than hematite nanoparticles, as shown in Fig. 7 by the INM sample that is mostly made of hematite.

These catalysts strongly deactivated during ethylbenzene dehydrogenation and achieved stable values after 4 h of reaction; at this time, magnesia and the IM sample showed close values. On the other hand, the magnesia-supported iron nanoparticles showed conversions above 20%, which is much higher than that of the commercial catalyst (10%), evaluated in the presence of steam [43]. The catalysts deactivation can be related to the changes that have been occurred during ethylbenzene dehydrogenation. As found by X-ray diffraction and Mössbauer spectroscopy, during reaction hematite has been changed to magnetite, resulting in solids with lower specific surface areas. As shown in Table 1, during reaction, magnesia went on sintering and a slight decrease in the specific surface area (14%) was noted but it was not enough to cause the catalyst deactivation. On the other hand, the decrease in the specific surface area for the IM (21%) and INM (33%) samples seems to contribute to deactivation. In addition, as found by Mössbauer spectroscopy, some $Fe^{3+}$ species went on magnesia lattice decreasing the iron active sites for the reaction, this effect being stronger for the IM sample, which has shown the strongest deactivation. Therefore, after 3 h of reaction this catalyst behaved like pure magnesia.

Table 4 shows the values of ethylbenzene conversion, styrene yield and of selectivities of styrene, benzene and toluene after 4 h on stream, during ethylbenzene dehydrogenation in the presence of carbon dioxide. It can be noted that the presence of iron led to an increase of styrene selectivity which increased even more when hematite is the predominant phase of the catalysts (INM sample).

All catalysts showed low selectivity to benzene and toluene, the main byproducts of ethylbenzene dehydrogenation and were more selective to toluene. This can be related to the basicity of the solids. It is known [44] that the acid–base and redox properties of the catalyst affect the conversion and selectivity of ethylbenzene to styrene. If the basic sites are strong enough to abstract the β-hydrogen of ethylbenzene, the rupture of the C–C lateral bond (263.7 kJ $mol^{-1}$) will be favored and thus the selectivity to toluene will increase. On the other hand, if the surface acidity is higher α-hydrogen can be abstracted from ethylbenzene and the rupture of the phenyl-C bond (364.2 kJ $mol^{-1}$) will be favored, resulting in an increase in selectivity to benzene.

## 4. Conclusions

The method of impregnating iron on magnesia affects the textural properties of these catalysts and their activity and selectivity in ethylbenzene dehydrogenation in the presence of carbon dioxide to produce styrene. By using the classical method of impregnation, a catalyst made of a spinel ($MgFe_2O_4$) co-existing with magnesia containing $Fe^{3+}$ species diffused in the lattice. This solid has higher

specific surface area and is more active and selective to styrene than magnesia. On the other hand, the deposition of iron nanoparticles through a magnetic fluid on magnesia produces a catalyst made of magnesia-supported hematite nanoparticles co-existing with magnesia containing $Fe^{3+}$ species diffused in the lattice. This solid shows specific surface area and activity even higher and is much more reducible than the other sample. These differences were related to the presence of hematite nanoparticles (18 and 71 nm), as well as to the lower tendency of iron species to diffuse into magnesia lattice in this catalyst, as compared to the other solid. From these results, we can conclude that the $Fe^{3+}$ species are more active and selective to styrene, in ethylbenzene dehydrogenation in the presence of carbon dioxide, when they are as hematite nanoparticles supported on magnesia than when they are in the environment of magnesium ferrite supported on magnesia.

## Acknowledgments

APMM, MSR and SBL acknowledge CAPES, FAPESB and CNPq for their graduate fellowships. The authors thank CNPq and FINEP for the financial support.

## References

[1] H.J. Herzog, Energy Econ. 33 (2011) 597–604.
[2] J. Koornneef, P.V. Breevoort, C. Hamelinck, C. Hendriks, M. Hoogwijk, K. Koop, M. Koper, T. Dixon, A. Camps, Int. J. Greenhouse Gas Control 11 (2012) 117–132.
[3] X. Zhao, X. Wang, Catal. Commun. 7 (2006) 633–638.
[4] M. Chen, J. Xu, Y.-M. Liu, Y. Cao, H.-Y. He, J.-H. Zhuang, Appl. Catal., A 377 (2010) 35–41.
[5] J.F. Ding, Z.F. Qi, S.-W. Chen, X.-K. Li, G.-F. Wang, J.-G. Wang, J. Fuel Chem. Technol. 38 (4) (2010) 458–461.
[6] S.B. Oliveira, D.P. Barbosa, A.P.M. Monteiro, D. Rabelo, M.C. Rangel, Catal. Today 133-135 (2008) 92–98.
[7] M.C. Rangel, A.P.M. Monteiro, M. Oportus, P. Reyes, M.S. Ramos, S.B. Lima, Ethylbenzene dehydrogenation in the presence of carbon dioxide over metal oxides, in: G.C. Liu (Ed.), Capturing, Utilization and Reduction Greenhouse Gases, InTech, USA, 2012, pp. 115–135.
[8] G.C. Araújo, S. Lima, M.C. Rangel, V.L. Parola, M.A. Penã, J.L.G. Fierro, Catal. Today 107–108 (2005) 906–912.
[9] X. Li, M.-G. Bai, X.-M. Tao, S.-Y. Shang, Y.-X. Yin, X.-Y. Dai, J. Fuel Chem. Technol. 38 (2) (2010) 195–200.
[10] M.M. Bhasin, J.H. McCain, B.V. Vora, T. Imai, P.R. Pujadó, Appl. Catal., A 221 (2001) 397–419.
[11] V.C. Corberán, Catal. Today 99 (2005) 33–41.
[12] C. Li, C. Miao, Y. Nie, Y. Yue, S. Gu, W. Yang, W. Hua, Z. Gao, J. Catal. 31 (2010) 993–998.
[13] E.A. Mamedov, Appl. Catal., A 116 (1994) 49–70.
[14] F. Cavani, F. Trifiro, Appl. Catal., A 133 (1995) 219–239.
[15] M.N.M. Barbosa, M.F.A. Carvalho, M.C. Rangel, Quim. Nova 20 (1997) 463–468.
[16] B.D. Herzog, H.F. Raso, Ind. Eng. Chem. Process Des. Dev. 23 (1984) 187–196.
[17] N. Mimura, M. Saito, Catal. Lett. 58 (1999) 59–62.
[18] N. Mimura, M. Saito, Catal. Today 55 (2000) 173–178.
[19] M. Saito, H. Kimura, N. Mimura, J. Wu, K. Murata, Appl. Catal., A 239 (2003) 71–77.
[20] T. Badstube, H. Papp, P. Kustrowski, R. Dziembaj, Catal. Lett. 55 (1998) 169–172.
[21] R. Dziembaj, P. Kustrowski, T. Badstube, H. Papp, Top. Catal. 11–12 (2000) 317–326.
[22] M.S. Park, J.-S. Chang, D.S. Kim, S.-E. Park, Res. Chem. Intermed. 28 (2002) 461–469.
[23] J.-S. Chang, D.-Y. Hong, Y.-K. Park, S.-E. Park, Stud. Surf. Sci. Catal. 153 (2004) 347–350.
[24] V.P. Vislovskiy, J.-S. Chang, M.-S. Park, S.-E. Park, Catal. Commun. 3 (2002) 227–231.
[25] M.-S. Park, V.P. Vislovskiy, J.-S. Chang, Y.-G. Shul, J.S. Yoo, S.-E. Park, Catal. Today 87 (2003) 205–212.
[26] T. Badstube, H. Papp, R. Dziembaj, P. Kustrowski, Appl. Catal., A 204 (2000) 153–165.
[27] Y. Sakurai, T. Suzaki, N.-O. Ikenaga, T. Suzuki, Appl. Catal., A 192 (2000) 281–288.
[28] A.S. Ivanova, Kinet. Catal. 46 (2005) 620–633.
[29] J.S. Moura, M.O.G. Souza, J.D.A. Bellido, E.M. Assaf, M. Opportus, P. Reyes, M.C. Rangel, Int. J. Hydrogen Energy 37 (2011) 3213–3224.
[30] M.S. Santos, S.G. Marchetti, A. Albornoz, M.C. Rangel, Catal. Today 133 (2008) 160–167.
[31] A.S.R. Medeiros, M.C. Rangel, Stud. Surf. Sci. Catal. 175 (2010) 815–818.
[32] M.S. Ramos, M.S. Santos, L.P. Gomes, A. Albornoz, M.C. Rangel, Appl. Catal., A 341 (2008) 12–17.
[33] M.S. Santos, S.G. Marchetti, A. Albornoz, M.C. Rangel, Stud. Surf. Sci. Catal. 175 (2010) 819–822.
[34] A. Oliveira, J.L.G. Fierro, M.C. Rangel, Catal. Today 85 (2003) 49–57.
[35] E. De Grave, A. Govaert, D. Chambaere, G. Robbrecht, Physica B 96 (1979) 103–110.
[36] R.E. Vandenberghe, E. De Grave, C. Landuydt, L.H. Bowen, Hyperfine Interact. 53 (1990) 175.
[37] S. Mørup, H. Topsøe, Appl. Phys. 11 (1976) 63–66.
[38] F. Bødker, S. Mørup, Europhys. Lett. 52 (2) (2000) 217–223.
[39] F.J. Berry, S. Skinner, M.F. Thomas, J. Phys. Condens. Matter 10 (1998) 215–220.
[40] P. Kustrowski, D. Sulkowska, L. Chmielars, A. Rafalska-Lasocha, B. Dudek, R. Dziembaj, Microporous Mesoporous Mater. 78 (2005) 11–22.
[41] J.R.C. Bispo, A.C. Oliveira, M.L.S. Corrêa, J.L.G. Fierro, S.G. Marchetti, M.C. Rangel, Stud. Surf. Sci. Catal. 142 (2002) 517–524.
[42] M.S. Santos, A. Albornoz, M.C. Rangel, Stud. Surf. Sci. Catal. 162 (2006) 753–760.
[43] R.D. Holtz, S.B. Oliveira, M.A.F.M.C. Rangel, Appl. Catal., A 350 (2008) 79–85.
[44] N. Dulamită, A. Măicăneanu, D.C. Sayle, M. Stanca, R. Crăciun, M. Olea, C. Afloroae, A. Fodor, Appl. Catal., A 287 (2005) 9–18.